

# Impacts of Anisotropic Porosity on Heat Transfer and Off-Gassing during Biomass Pyrolysis

M. Brennan Pecha,\* Nicholas E. Thornburg, Chad A. Peterson, Meagan F. Crowley, Xi Gao, Liqiang Lu, Gavin Wiggins, Robert C. Brown, and Peter N. Ciesielski

Cite This: *Energy Fuels* 2021, 35, 20131–20141

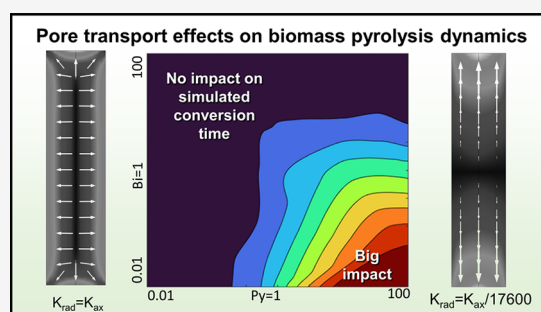
Read Online

ACCESS |

Metrics & More

Article Recommendations

**ABSTRACT:** The pore structure of biogenic materials imbues the ability to deliver water and nutrients through a plant from root to leaf. This anisotropic pore granularity can also play a significant role in processes such as biomass pyrolysis that are used to convert these materials into useful products like heat, fuel, and chemicals. Evolutions in modeling of biomass pyrolysis as well as imaging of pore structures allow for further insights into the concerted physics of phase change-induced off-gassing, heat transfer, and chemical reactions. In this work, we report a biomass single particle model which incorporates these physics to explore the impact of implementing anisotropic permeability and diffusivity on the conversion time and yields predicted for pyrolysis of oak and pine particles. Simulation results showed that anisotropic permeability impacts predicted conversion time more than 2 times when the Biot number is above 0.1 and pyrolysis numbers ( $Py_1$ ,  $Py_2$ ) are less than 20. Pore structure significantly impacts predicted pyrolytic conversion time (>8 times) when the Biot number is above 1 and the pyrolysis number is below 1, i.e., the “conduction controlled” regime. Therefore, these nondimensional numbers reflect that when internal heat conduction limits pyrolysis performance, internal pyrolysis off-gassing further retards effective heat transfer rates as a closely coupled phenomenon. Overall, this study highlights physically meaningful opportunities to improve particle-scale pyrolysis modeling and experimental validation relevant to a variety of feedstock identities and preparations, guiding the future design of pyrolyzers for efficient biomass conversion.



## 1. INTRODUCTION

Fast pyrolysis of biomass is a unique technology for converting lignocellulosic materials into biocrude oil, char, and combustible gases. Rapid cooling of the condensable products preserves many of the biomolecular chemical bonds before they reach thermodynamic equilibrium and fully convert to syngas and carbon rich char. The condensable pyrolysis vapors can be converted into liquid transportation fuels through a variety of catalytic processes involving vapor-phase upgrading<sup>1,2</sup> and hydrotreating.<sup>3</sup> The yield and quality of the bio-oil depend strongly on the composition, particle size, and density of biomass as well as on the reactor conditions that dictate the heat transfer and time that the material resides in the hot reactor—whether an inert gas or a small amount of oxygen is used.<sup>4–6</sup> In general, the highest oil yields and best quality are achieved using small particle sizes that minimize intraparticle heat transfer limitations, continuous mixing, and short vapor residence times.<sup>7–9</sup> As such, fluidized bed and entrained flow reactors are often used for fast pyrolysis.<sup>10</sup>

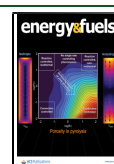
Design parameters for a pyrolysis system include not only the reactor’s dimensions and operating conditions but also selection of pretreatments such as grinding, drying, or adding

in a catalyst. At a fundamental level, pyrolysis models must capture the four key translational physics that span the particle scale to reactor scale: heat transfer, mass transfer, chemical reactions, and phase change.<sup>11</sup> Laboratory experiments often isolate one of these phenomena to extract useful modeling parameters—for example, using a thin film of wood or cellulose to evaluate chemical reaction rate parameters in the absence of particle heat transfer limitations.<sup>12–14</sup> However, the other coupled physics must also be captured to accurately predict conversion times which are critical to properly size a pyrolysis reactor, which in turn contributes a significant capital cost in a biorefinery.<sup>15,16</sup> For example when using larger particles that take longer to pyrolyze, reactors must accommodate a larger volume of biomass to reach full conversion and must thus be bigger.<sup>17</sup> Multiscale modeling approaches that comprise

Received: August 6, 2021

Revised: November 23, 2021

Published: December 6, 2021



intraparticle transport and the local internal/external environments that the particle experiences are key to achieving this goal.<sup>11,18–20</sup>

Early pyrolysis models relied on low-order approximations of heat transfer within the biomass particle and surface heat transfer to predict conversion times and yields, for example, Pyle's and Zaror's work developing nondimensional pyrolysis numbers.<sup>21</sup> One-dimensional (1D) models introduced intraparticle gradients and greatly improved the accuracy, especially when using nonspherical coordinates like cylinder radius, for example Van de Velden et al.'s work.<sup>13</sup> Two- (2D) and three-dimensional (3D) models allowed for the study of anisotropic physical transport, which is inherent to lignocellulosic materials that have highly directional porosity. Examples of these types of models include the works of Di Blasi<sup>22–24</sup> with a simplistic biomass reaction scheme and others that can capture bio-oil quality by using multistep, multicomponent reaction schemes like the CRECK variants.<sup>25–28</sup> Indeed, 3D combustion modeling of whole logs has been performed with great predictive capacity.<sup>29</sup> While high in computational cost compared to 1D or 0D models, these multidimensional models have been coupled to high-fidelity reactor simulations either directly or indirectly as a calibration for lower-order particle models or for other mathematical methods.<sup>10,30,31</sup>

The anisotropy native to lignocellulosic is imbued by the porous tissue structure of the once living organism. Key properties that emerge from this nature include particle shape (resultant from comminution), thermal conductivity, diffusivity, and permeability. Predictions of thermal gradients become more accurate as the particle geometry is represented with greater fidelity as the particle shape impacts both internal heating depth and external surface area.<sup>32,33</sup> Thermal conductivity in the longitudinal direction of wood can be as high as 3 times the radial direction with respect to grain<sup>34</sup> and between 1.5–2.5 times for pine.<sup>35</sup> Many models have shown that under relevant fast pyrolysis conditions, anisotropic conductivity plays a key role in predicting conversion time and yield, wherein axial heat transfer is much faster than radial due to pore connectivity.<sup>26,36</sup> However, there is some conflicting information regarding the impact of incorporating directional permeability into particle models. The directional gas permeability of wood is strongly dependent on pore structure. Comstock measured gas permeabilities in the longitudinal direction, demonstrating some of the earliest quantitative evidence of this phenomenon.<sup>37</sup> Despite this, others have concluded that permeability plays very little role in pyrolysis simulations, and as such, many models do not account for directional permeability.<sup>26,36</sup> One work from Di Blasi reports a mass source term in the Navier–Stokes equations and found that when using tangential and radial permeabilities convective flow out of the particle due to the pyrolysis phase-change reactions impacts heat transfer to the particle wall, as outflowing gases travel counter to heat migration.<sup>38</sup> In this work, Di Blasi assumed that axial permeability is 1000 times higher than radial permeability for a 2D model to represent grain structure and compares this to a 1D model for wood with isotropic properties. The conclusion was that as particle sizes become larger, convective heat transfer plays less of a role than internal conductive heat transfer. However, a systematic evaluation of the isolated impacts of anisotropic permeability with all else in the model remaining constant was not performed.

Moreover, biomass shrinkage plays an impactful role in pyrolytic conversion. As mass is lost from the phase-change reactions, the density of the particle drops—but so does the volume of the particle. This is especially important to capture in fluidized systems wherein accurate density and particle size is coupled to a drag model to track the particle's location and residence time.<sup>10</sup> For experiments with a fixed particle, the drag model is not relevant, but shrinking still plays a notable role in the surface area and density which imbue changes to the convective heat transfer and internal solid thermal conductivity, respectively. Accordingly, there are many ways to account for biomass shrinkage. Some authors have even used 3D modeling to directly resize particles during conversion, although this approach is computationally intensive.<sup>26</sup> In an effort to balance simulation time with key parameters impacted by shrinkage, an implicit shrinkage model is applied in this work to dynamically rescale the convective heat transfer coefficient and internal thermal conductivity with conversion. This selection was made because heat transfer, internal or external, has been repeatedly determined to control the effective pyrolysis rate under relevant fast pyrolysis conditions.<sup>21,39,40</sup>

In this work, we follow up on the work of Di Blasi et al.<sup>38</sup> to evaluate the impacts of physical permeability on pyrolysis conversion behavior to understand when this transport phenomenon is important to include in particle simulations and, importantly, when it can be ignored. Nondimensional analysis is used to explore the relevant parameter space and to draw insights from comparisons to experimental pyrolysis data for an oak cylinder.

## 2. METHODS

**2.1. Particle-Scale Model.** A single particle model for a particle of wood is used in this work to predict yields from the various critical material attributes described in this work. Finite element method (FEM) software COMSOL Multiphysics 5.6 was utilized to perform numerical time-dependent simulations. A 2D axisymmetric model describes a finite cylinder, which is more accurate than spherical assumptions of biomass particles<sup>41</sup> and allows for morphologically relevant anisotropic transport. The model incorporates simultaneous multispecies reaction, mass transport, and heat transport equations with convection possible within the particle due to pressure gradients resulting from pyrolysis phase changes. The pyrolysis reaction scheme, species heat capacities, molecular weights, and Arrhenius-type rate constants were taken from Debiagi et al.,<sup>25</sup> as this scheme has been validated across a variety of biomass feedstocks and can input compositional analysis as initial values. Parametric sweeps were performed over a variety of initial conditions describing various temperatures, initial compositions, ash contents, initial moisture contents, and particle sizes. The mesh for the 2D axisymmetric model has 2064 domain elements and 220 boundary elements, as shown in Figure 1.

**Mass and Momentum Transfer Equations.** The permeability of the wood has axial and radial components. Comstock<sup>37</sup> measured directional gas permeabilities for pine wood. Axial permeability for pine can be taken as  $1.08 \times 10^{-11} \text{ m}^2$  when scaled for SI units, and the radial permeability was measured to be 17,600 times smaller, at  $6.18 \times 10^{-16} \text{ m}^2$ . Permeability is thus represented as a diagonal tensor and incorporated into the modified Brinkman equation which describes conservation of momentum for transient low Mach number compressible fluid within the porous biomass particle

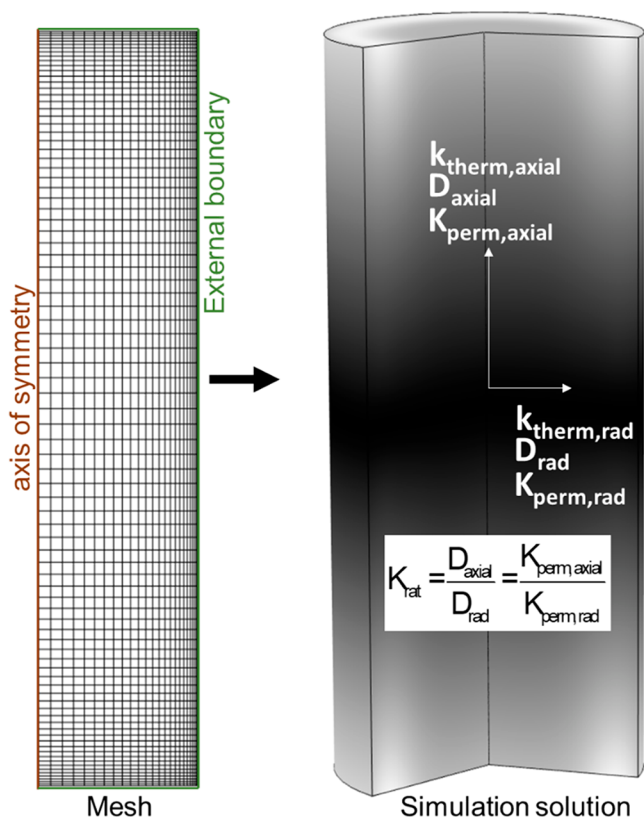


**Figure 1.** Mesh for the 2D axisymmetric particle model (left). The software calculates transport for a full 3D volume rotated around the axis in its calculations (3D cutaway at right) with definitions for key anisotropic physical parameters corresponding to wood's granular macropore structure.

**Table 1.** General Parameters Used in Particle Pyrolysis Models

Description	Constant/calculation	Comment
$\rho_{wood\_wall}$	1500 kg/m <sup>3</sup>	density of the wood and char cell wall (i.e., without macroporosity) <sup>46</sup>
$\rho_{ash}$	$\frac{(1 - \epsilon_{p,0})\gamma_{ash,0}\rho_{wood\_wall}}{(1 - \gamma_{ash,0})}$	density of ash component estimated as mass fraction of cell wall density for wood
$k_{cell\_wall}$	$(0.0159 + 7.36 \times 10^{-4} \times T/0.8 [K])$ W/mK	thermal conductivity of wood/char cell wall solid fraction <sup>47</sup>
$k_{char,wall}$	1 W/m K	thermal conductivity of char wall (est.)
$k_{moisture}$	0.61 W/m K	thermal conductivity of liquid water
$k_{ash}$	1 W/m K	thermal conductivity of ash in cell wall (est. from glass)
$k_{radial}/k_{axial}$	1.78	axial thermal conductivity is higher than radial in wood <sup>26</sup>
$C_{p,ash}$	0.84 J/g K	heat capacity of ash (est. from sand)
$K_{ax}$	$1 \times 10^{-12}$ m <sup>2</sup>	axial permeability of wood <sup>37</sup>
$D_{gas}$	$3 \times 10^{-5}$ m <sup>2</sup> /s	diffusion coefficient for all gases
$V_f/V_0$	0.55	final vs initial particle volume due to shrinkage calculated from oak pyrolysis images

**Table 2.** Particle Proximate Analysis<sup>a</sup>

Proximate analysis	wt %
Moisture	5.65 [0.18]
Volatile matter	74.74 [0.79]
Fixed carbon	19.30 [0.87]
Ash	0.31 [0.17]

<sup>a</sup>Sample standard deviation is in brackets. Analysis was repeated with four replicates.

$$\frac{1}{\epsilon_g} \rho_g \frac{d\mathbf{u}}{dt} + \frac{1}{\epsilon_g} \rho_g (\mathbf{u} \cdot \nabla) \mathbf{u} - \frac{1}{\epsilon_g} \nabla \cdot [-p\mathbf{I} + \mathbf{Y}] - \left( \mu \mathbf{K}^{-1} + \frac{\nabla \cdot (\rho_g \mathbf{u})}{\epsilon_g^2} + \frac{Q_m}{\epsilon_g^2} \right) \mathbf{u} \quad (2)$$

where

$$\mathbf{Y} = \mu \frac{1}{\epsilon_g} (\nabla \mathbf{u} + (\nabla \mathbf{u})^T) - \frac{2}{3} \mu \frac{1}{\epsilon_g} (\nabla \cdot \mathbf{u}) \quad (3)$$

where  $\epsilon_g$  is the wood particle macroporosity,  $\rho_g$  fluid density,  $\mathbf{u}$  fluid velocity vector,  $\mu$  fluid viscosity,  $\mathbf{I}$  the identity matrix,  $\mathbf{K}$  the permeability tensor for the wood particle, and  $Q_m$  the mass source term from the pyrolysis phase change. Mass conservation of the gas phase is upheld by the relationship

$$\frac{d\epsilon_g \rho_g}{dt} + \nabla \cdot (\rho_g \mathbf{u}) = Q_m \quad (4)$$

and for the solid phase

$$\frac{d(1 - \epsilon_g) \rho_s}{dt} = -Q_m \quad (5)$$

The mass source term  $Q_m$  is determined from the wood/intermediates/char to vapor/gas reaction rates in units of kg/m<sup>3</sup> s

$$Q_m = \sum_j R_j M_{w,j} \quad (6)$$

where  $j$  is the vapor/gas species,  $R_j$  the reaction rate of production for species  $j$ , and  $M_{w,j}$  the molecular weight of species  $j$ . Porosity changes as a function of conversion

$$\epsilon_g = 1 - (1 - \epsilon_{g,0}) \frac{\rho_s}{\rho_{s,0}} \quad (7)$$

where the density of the solid is the sum of all solid species  $i$  densities following the Debiagi scheme

$$\rho_s = \sum_i C_i M_{w,i} \quad (8)$$

where  $C_i$  is the concentration of solid species  $i$ . The density of the vapor phase is calculated from the ideal gas law

$$\rho_g = \frac{p M_{w,vap}}{RT} \quad (9)$$

where

$$M_{w,g} = \frac{\sum_j C_j M_{w,j}}{\sum_j C_j} \quad (10)$$

and  $C_j$  is the concentration of vapor species  $j$ ,  $R$  the universal gas constant, and  $T$  the temperature. The outer boundary condition for the particle surface (Figure 1) was set to a constant pressure.

**Heat Transfer Equations.** Conservation of energy is achieved with the following equations described in terms of temperature, assuming ideal gas behavior and negligible viscous heating

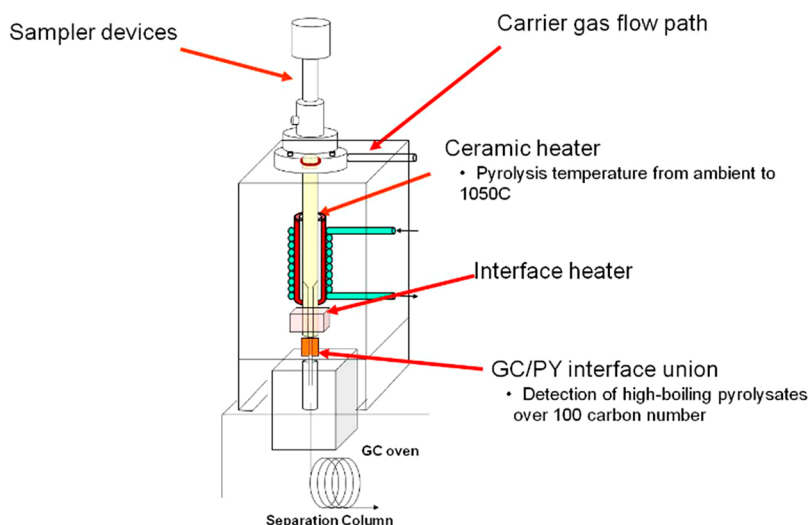


**Figure 2.** Schematic of the Frontier micropyrolyzer used for the single particle experiments.

$$(\rho_g c_p)_{\text{eff}} \frac{\partial T}{\partial t} + \rho_g c_p \mathbf{u} \cdot \nabla T - \nabla \cdot \mathbf{k}_{\text{eff}} \nabla T = \dot{Q} \quad (11)$$

where

$$(\rho_{\text{total}} c_p)_{\text{eff}} = \varepsilon_g \rho_g c_{p,g} + (1 - \varepsilon_g) \rho_s c_{p,s} \quad (12)$$

and

$$\mathbf{k}_{\text{eff}} = \varepsilon_g \mathbf{k}_g + (1 - \varepsilon_g) \mathbf{k}_s \quad (13)$$

where subscript *s* indicates solid cell wall phase and subscript *p* porous gas/vapor phase;  $\rho$  is density,  $\mathbf{k}$  thermal conductivity tensor,  $Q$  the heat source term,  $T$  the temperature, and  $c_p$  heat capacity of the gas, *g*, and solid, *s*, fractions. The heat source term refers to the sum of the heats of each reactions ( $H$ ) of index  $x$  associated with each species  $j$

$$\dot{Q} = \sum_x C_p M_{w,j} k_x \Delta H_x \quad (14)$$

The particle surface allows for convective heat flux with a heat transfer coefficient to describe heat transfer from implicit flowing of gas over the solid

$$-n \cdot q = (T_{\text{inf}} - T)h \quad (15)$$

where  $q$  is normal flux into or out of the surface of the particle. The surface heat transfer coefficient  $h$  was calculated following the method described by Tavassoli et al.<sup>42</sup> for nonspherical biomass particles. A previous study has shown that using a heat transfer coefficient may be a more appropriate method for approximating surface heat transfer than direct numerical simulation of gases flowing around the particle due to orientation effects.<sup>43</sup>

Thermal conductivities for CO, CO<sub>2</sub>, H<sub>2</sub>, H<sub>2</sub>O, N<sub>2</sub>, and C<sub>6</sub>H<sub>6</sub> were taken from Coker,<sup>44</sup> Appendix C. Gas-phase thermal conductivities are not available for the majority of the pyrolysis products, so all unknowns were estimated to be the same as C<sub>6</sub>H<sub>6</sub>. The overall gas thermal conductivity was density-averaged for gas phase species and represents a much smaller thermal mass than the solids due to density. The thermal conductivity of the solid phase was taken as density-weighted average of the wood, char, moisture, and ash contributions. Heat capacities for each species were reported as a function of temperature by Debiagi et al.<sup>25</sup>

$$c_{p,s} = \frac{\sum_i c_{p,i} C_i}{\rho_s} \quad (16)$$

and

$$c_{p,g} = \frac{\sum_j c_{p,j} C_j}{\rho_g} \quad (17)$$

**Implicit Shrinkage Model.** The Bellais model for 2D shrinking<sup>45</sup> was used in this work and is apt for the two cylindrical validation cases utilized herein. The final volume ( $V_{p,f}$ ) of the particle when scaled by the shrinkage constants in the radial (subscript *r*) and length (subscript *z*) directions is

$$V_{p,f} = V_{p,0} (1 - s_{r,\text{char}})^2 (1 - s_{z,\text{char}}) \quad (18)$$

where  $s_{r,\text{char}}$  and  $s_{z,\text{char}}$  are 0.224 and 0.098, respectively, scaled equally from Bellais' values to meet 45% volumetric shrinkage.<sup>28</sup> At zero conversion, the initial particle volume is

$$V_{p,0} = \pi r^2 L \quad (19)$$

where  $r$  is particle radius, and  $L$  is particle length. The final surface area of the particle is therefore

$$A_{s,f} = 2\pi r L (1 - s_{r,\text{char}})(1 - s_{z,\text{char}}) + 2\pi (r(1 - s_{r,\text{char}}))^2 \quad (20)$$

where  $A_{s,f}$  is surface area for a completely pyrolyzed particle. The surface area for an unconverted particle is

$$A_{s,0} = 2\pi r L + 2\pi r^2 \quad (21)$$

Conversion,  $\alpha$ , is calculated defined by the following equation

$$\alpha = 1 - \left( \frac{\rho_{\text{wood,daf}}}{\rho_{\text{wood,daf},0}} \right) \quad (22)$$

where  $\rho_{\text{wood,daf}}$  is the density of primary pseudospecies and primary intermediates CELL, CELLA, GMSW, HCE1, HCE2, LIG, LIGC, LIGCC, LIGH, LIGO, LIGOH, TANN, TGL, XYGR, and XYHW.<sup>25</sup> The value for  $\rho_{\text{wood,daf},0}$  is at the initial conditions. The relative change in volume at any given time  $t$  is therefore

$$V_{p,t} = \alpha \left( 1 - \frac{V_{p,f}}{V_{p,0}} \right) \quad (23)$$

while the relative change in surface area at time  $t$  is given as

$$A_{s,t} = \alpha \left( 1 - \frac{A_{s,f}}{A_{s,0}} \right) \quad (24)$$

Using these expressions, the thermal conductivity is amplified by the volumetric densification and heat transfer coefficient  $h$  from eq 13 is attenuated by the surface area change of particle shrinking.

**Chemical Species Transport Equations.** The Debiagi reaction scheme<sup>25</sup> utilizes pseudospecies to represent cellulose, hemicellulose, lignin, and extractives with stoichiometric balance, heat of reaction for each step, and Arrhenius style rate constants. Bio-oil yields were taken as the sum of the 23 “bio-oil” assignments, gas yields from the six “bio-gas”, and biochar as a sum of all the solid and metaplastic species and ash remaining in the solid.

Initial concentrations for each solid pseudospecies (cellulose, lignins, hemicelluloses, and extractives) were calculated with respect to the density of the dry wood cell wall

$$C_{i,0} = (1 - \epsilon_{g,0})\rho_{wood\_wall}y_i/M_{w,i} \quad (25)$$

In the solid domain, the solid species do not advect or diffuse, so the equation describing their transport is

$$\frac{\partial c_i}{\partial t} = R_i \quad (26)$$

where  $R_i$  is consumption or production of each pseudospecies  $i$ . Ash is considered to all remain in the solid, and water is assumed to be adsorbed and unable to diffuse until evaporated, treated as a chemical reaction in the Debiagi scheme. For the bio-oil, water vapor, and biogas species, the following equation describes transport in the porous void fraction of the wood

$$-\nabla \cdot \mathbf{D}_{eff,i} \nabla c_i + \mathbf{u} \cdot \nabla c_i = R_i \quad (27)$$

where

$$\mathbf{D}_{eff,i} = \epsilon_g \mathbf{D}_i \quad (28)$$

and  $\mathbf{D}_i$  is the fluid diffusivity tensor within the granular porosity. Within the porous fluid phase, the radial diffusion is slower in the radial direction than axial due to the pore directionality of biomass and char and is set to the same tensorial ratio as the permeability,  $K_{rat}$ . The outer surface of the particle as assigned a uniform fixed-gradient Robin boundary condition:

$$n \cdot \mathbf{D}_i \nabla c_i = 0 \quad (29)$$

Further parameters used in the simulations are listed in Table 1.

**2.2. Oak Cylinder Pyrolysis.** To provide consistent particles for experimentation and model validation (versus heterogeneous particles from a hammer mill), red oak dowels were prepared. The starting “feedstock” was 5/16 in. red oak dowel rods from Baird Brothers Fine Hardwoods in Ames, Iowa. By starting with prefabricated dowels, feedstock preparation was simplified. Using a dowel plate and drill press, the 5/16 in. dowels were trimmed to a diameter of 3 mm. Then, the 3 mm diameter rods were cut to a length of  $\sim 12$  mm producing a set of uniformly sized single particles. The proximate analysis for this sample is shown in Table 2.

A Frontier micropyrolyzer (PY-3030) was used to conduct the single particle experiments. Modifications were made to the system allowing for quenching of the pyrolysis products as outlined in the work of Lindstrom et al.<sup>48</sup> Flow into the reactor was controlled by a mass flow controller (Alicat: MC-500SCCM). For all experiments, helium was used as the reference gas in the flow controller.

For the experiments, the particles were dried at 105 °C for 5 h to drive off any moisture. Then, the particles were weighed and measured (height and diameter). The particles were then placed in a desiccant container to avoid absorbing any moisture from the ambient air. Immediately preceding the experiments, a single particle was removed from the desiccant container. Then, a stainless-steel metal harness was prepared holding the particle. This harness was used to suspend the particle in the reactor zone. The particle was lowered into the reactor using the micropyrolyzer’s sample holder.

After rapidly lowering the particle into the reactor zone, it was kept in the heated furnace for a predetermined time. After the set duration, the particle was dropped into a either a water bath or a water saturated Kimwipe to prevent smoldering of the hot char in air. The particles were then dried at 105 °C following these quenching reactions for 4 h to drive off any moisture absorbed. The samples were then weighed immediately after this drying (to avoid saturation from

water in the air) and the mass recorded. After the mass was recorded, the samples were put into a tray and sealed for future analysis.

While the pyrolyzer was operated at a constant temperature of 500 °C (analytical interface temperature of 350 °C), large temperature gradients were measured in the system. Using the gas inlet as the datum reference (i.e., distance = 0 mm, designated as carrier gas flow path in Figure 2), only a small region was determined to be isothermal. Thus, efforts were made to consistently suspend the particles between a distance of 70–85 mm from the gas inlet (temperature 500–510 °C) to achieve  $\pm 20$  K thermal gradient. Triplicate experiments were performed for each of the five time steps: 0, 5, 20, 60, and 90 s.

### 3. RESULTS

#### 3.1. Model Validation: Oak Cylinder Pyrolysis at 500 °C.

Red oak dowels, 12 mm long and 3 mm diameter, were

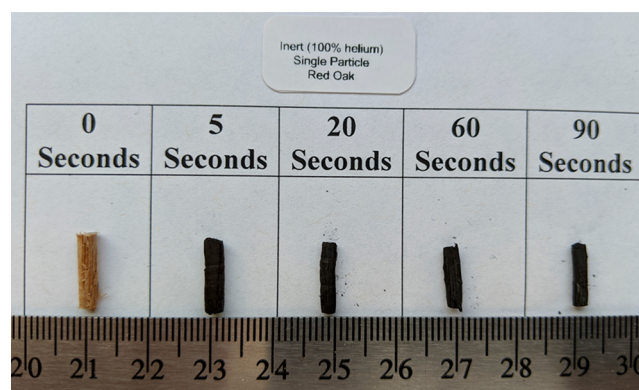
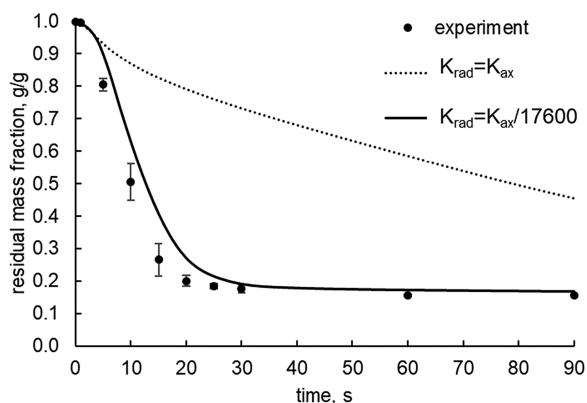


Figure 3. Red oak cylinder particles pyrolyzed for 0, 5, 20, 60, and 90 s.

Table 3. Parameters Utilized in Models for Oak Cylinders and Various Pine Simulations

Parameter	Oak cylinder (experiment)	Pine, various (theoretical)
$T_{gas,reactor}$ °C	500	500
$T_{particle,t=0}$ °C	120	
gas environment	He	N <sub>2</sub>
$p_{gas,reactor}$ kPa	101	143
$\epsilon_{g,0}$	0.49	0.56
$\rho_{particle,0}$ kg/m <sup>3</sup>	765	656
$r_{particle}$ mm	1.5	$1.53 \times 10^{-4}$ to 0.08
$L_{particle}$ mm	12	$10 \times$ radius
moisture content	0	0.06
ash content	0.0031	0.006
CELL	0.44	0.39
GMSW	0.34	0.25
LIGC	0	0
LIGH	0.11	0.18
LIGO	0.11	0.11
TANN	0	0
TGL	0	0.06
$h$ , W/m <sup>2</sup> K	359	92.5
$V_i/V_0$	0.46	0.46
$s_{r,char}$	0.224	0.224
$s_{z,char}$	0.098	0.098
$\mu_{g}$ Pa s	$3.85 \times 10^{-5}$	$3 \times 10^{-5}$
$k_{thermal,g}$ W/m K	0.1513	0.057
$c_{p,g}$ J/mol K	12.5	31.2



**Figure 4.** Residual mass fraction vs time for oak cylinder pyrolysis with two permeability tensor ratios.

pyrolyzed in a micropyrolyzer and weighed at 5-s intervals up to 30 s, then 30-s intervals up to 90 s with a final char yield of 16 wt %. 95% conversion based on equilibrium char yield was achieved by 25 s. Figure 3 shows photographs of particles at these time steps. The model was parametrized according to the values presented in Table 3. Two simulation cases were performed: one with isotropic permeability and diffusivity ( $1 \times 10^{-12} \text{ m}^2$  and  $6 \times 10^{-6} \text{ m}^2/\text{s}$  with  $e_{p0}$ , respectively, in all directions) and one with the radial permeability and diffusivity attenuated by a quotient factor of 17,600, as reported in gas permeability measurements by Comstock. The transport of momentum and species increase with increasing porosity as the biomass pyrolyzes, so permeation and diffusion accelerate with conversion. Simulation results show that while the anisotropic simulation captures mass conversion time within 5 s error, the isotropic simulation ( $K_{\text{rad}}=K_{\text{ax}}$ ) reveal a dramatic under-prediction of conversion as a function of time, as depicted in Figure 4.

Di Blasi<sup>49</sup> noted that isotropic permeability is unrealistic as it does not reflect the directional porosity of real biomass, for as vapors are formed during pyrolysis they will eject from the side

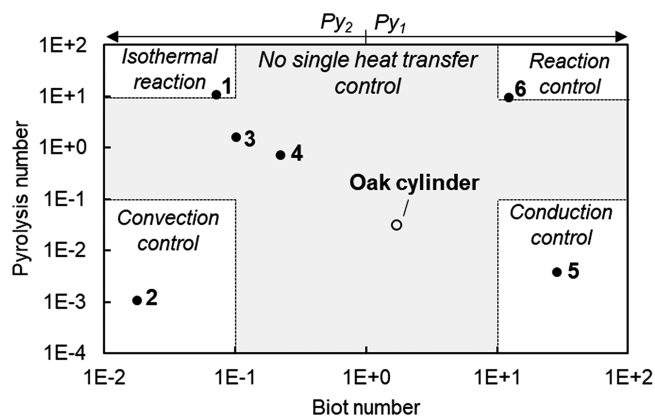


**Figure 6.** (A) Pyrolysis regime map corresponding to select test case simulations in this work.  $Bi > 1$ , is  $Py_1$  used;  $Bi < 1$ ,  $Py_2$  is used.

walls of a particle. This effect is especially amplified here by high  $L/D$  ratios of 4, wherein the surface area of the side walls account for 8 times that of the particle ends. The isotropic simulation does not even reach equilibrium pyrolysis conversion by the 90 s mark with residual mass of 45% remaining. Further exploration of this phenomenon can be seen in Figure 5 comparing the fluid velocities and surface temperatures for both simulations at the 20 s mark. While the fluid velocity reaches as high as 0.22 m/s ( $U_{\text{max}}$ ) leaving the anisotropic simulation primarily directed toward the particle ends, the fluid velocity is directed in all directions for the isotropic simulations and maximizes at  $5 \times 10^{-3} \text{ m/s}$ . This outward moving convective flow of evolved pyrolysis gases absorbs heat along its path outward. This effectively suppresses the heat conducting through the solid radially, and indeed, we see that the temperature throughout the particle is approximately 100 K lower for the isotropic simulation. It should be noted that the Biot number is 1.7,  $Py_1$  0.03, and  $Py_2$  0.06, which places it in the intermediate noncontrolled regime but close to the conduction-controlled domain. Further discussion on these nondimensional numbers can be found

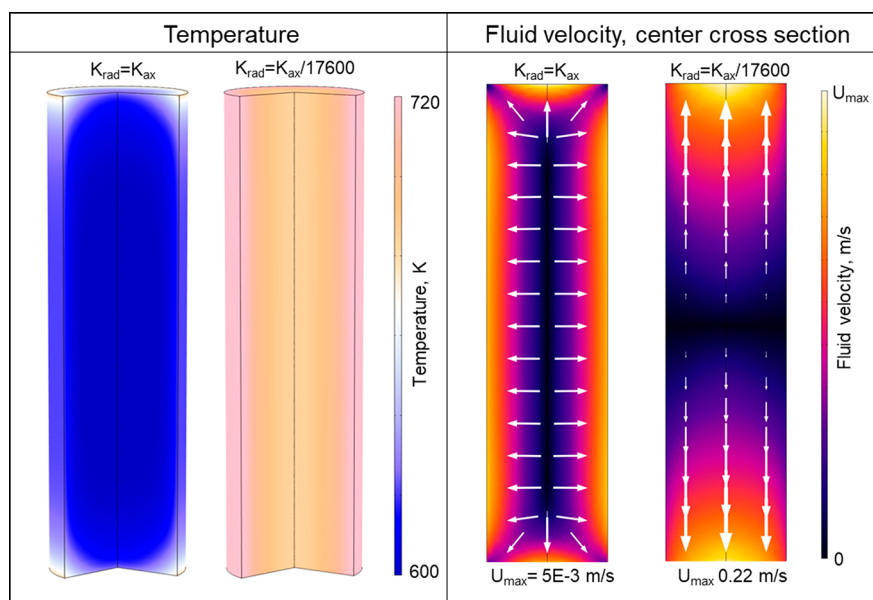


**Figure 5.** Temperature gradient (left) and intrapore fluid velocity (right) for the simulation of a pyrolyzing oak pellet at the 20 s mark for two different permeability conditions: isotropic ( $K_{\text{rad}} = K_{\text{ax}}$ ) and anisotropic ( $K_{\text{rad}} = K_{\text{ax}}/17,600$ ).

Table 4. Case Studies for Particles Pyrolyzing under Different Conditions as Reflected in the Nondimensional Numbers

	$r$ (m)	$L$ (m)	$h$ (W/m <sup>2</sup> K)	Bi	$Py_1$	$Py_2$	Regime description
1	$3.4 \times 10^{-4}$	$3.4 \times 10^{-3}$	92.5	0.22	3.3	0.73	Isothermal reaction
2	$2.5 \times 10^{-3}$	$2.5 \times 10^{-2}$	1	0.02	0.06	0.001	Convection controlled
3	$1.5 \times 10^{-4}$	$1.5 \times 10^{-3}$	92.5	0.10	16	1.6	No control
4	$5 \times 10^{-5}$	$5 \times 10^{-4}$	200	0.07	149	10.7	No control
5	$1 \times 10^{-2}$	0.1	400	29	$3.7 \times 10^{-3}$	0.11	Conduction controlled
6	$2 \times 10^{-4}$	$2 \times 10^{-3}$	1E4	12	9.4	116	Reaction controlled
Oak validation	$3 \times 10^{-3}$	$2.4 \times 10^{-2}$	92.5	1.7	$3.1 \times 10^{-2}$	$2.0 \times 10^{-5}$	No control

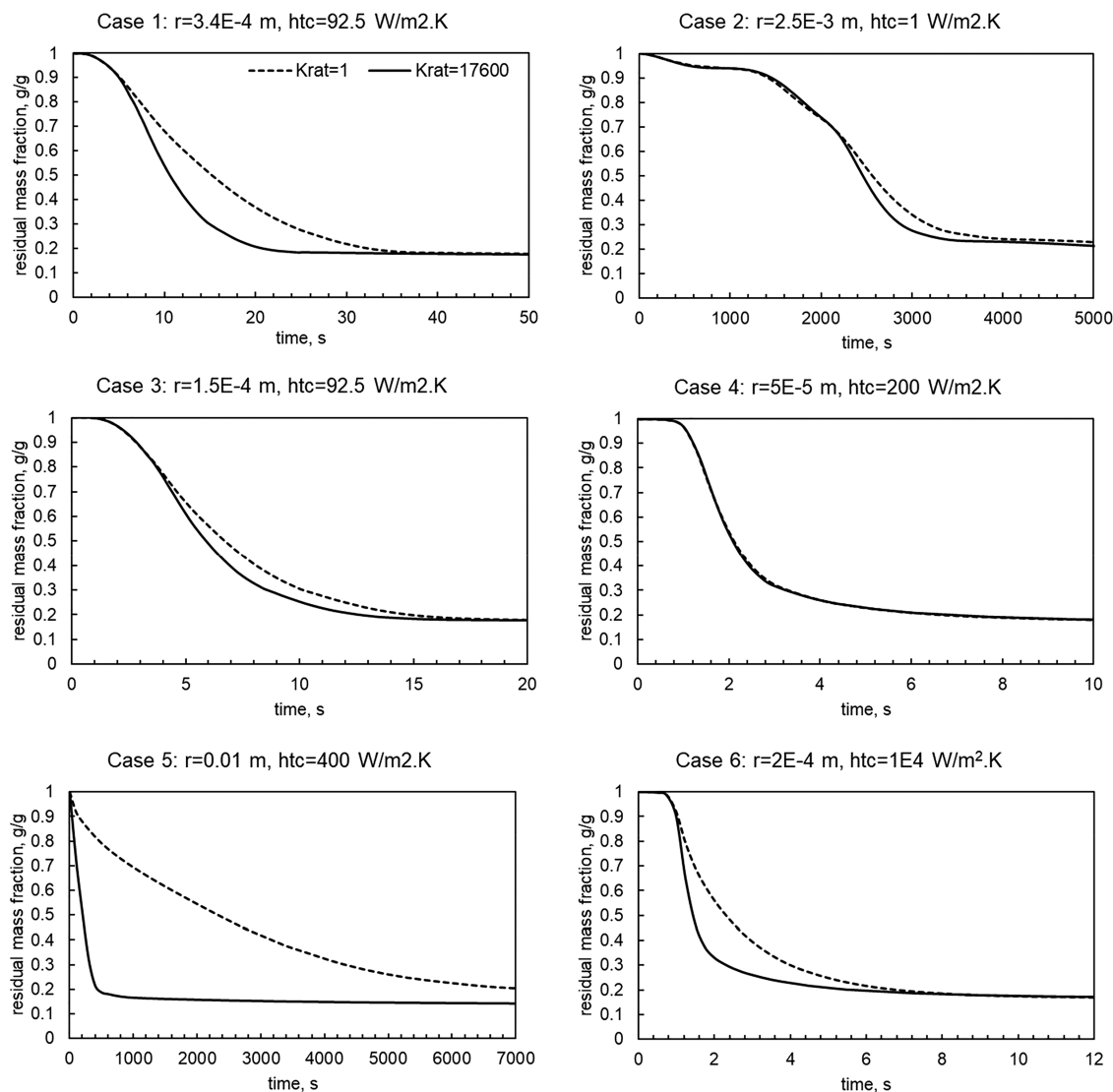


Figure 7. Residual mass fraction vs time excursions for case studies 1–6 across the pyrolysis regime map to elucidate the impacts of isotropic (dotted curves) vs anisotropic (solid curves) permeability assumptions on predicted conversion.

in the next section. While Di Blasi concludes that anisotropic permeability effects are minimal for particles in this regime, these results with high  $L/D$  show the contrary. Wardach-Święcicka and Kardaś<sup>50</sup> noticed in their simulations of wood that the advection of gases leaving wood particles during pyrolysis greatly reduces the particle heating rate compared with ignoring the critical phase change phenomenon. However, this work did not incorporate anisotropic pore structure via a permeability tensor.

### 3.2. Pyrolysis Regimes That Are Most Impacted by Anisotropic Permeability.

While the large oak particle

validation demonstrates the importance of anisotropic permeability, it is important to consider that this is a relatively large particle at 3 mm diameter and 12 mm length. In typical bench-scale fluidized bed reactors, 0.5–2 mm diameter particles are more common in fast pyrolysis experiments. However, particle size alone does not determine the so-called “pyrolysis regime”. In order to determine the pyrolysis regime, three nondimensional numbers are commonly calculated based on the particle size and environmental conditions. First, the Biot number  $Bi$  characterizes the ratio of convective heat to conductive heat

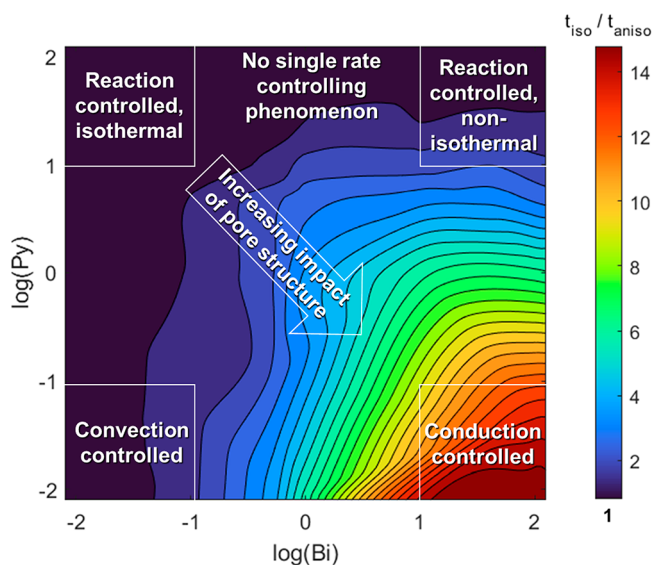


**Figure 8.** Regime map for relative 99% conversion time of simulations with isotropic porosity properties ( $t_{iso}$ ) over more realistic anisotropic properties ( $t_{aniso}$ ) based on 158 simulations with an interpolated color map. Log base 10.

**Table 5. Summary of Domains Wherein Grain-Oriented Off-Gassing Impacts Predicted Conversion Times during Wood Pyrolysis**

Bi	Py	Impact from grain-oriented off-gassing on pyrolysis conversion rates
<0.1	or $Py_{1/2} > 20$	Minimal to negligible
>0.1	and $Py_{1/2} < 20$	Notable impact
>1	and $Py_1 < 1$	Significant impact

$$Bi = \frac{h_{conv}r}{k_{cond}} \quad (30)$$

Next, the two pyrolysis numbers developed by Pyle and Zaror<sup>21</sup> compare heat transfer with an effective reaction rate at the external set fluid temperature. The first pyrolysis number  $Py_1$ , eq 31, compares conductive heat transfer to the effective reaction rate as estimated by the Di Blasi single step primary devolatilization rate<sup>51</sup> with  $A = 4.38E9$  1/s and  $E_a = 148$  kJ/mol. The single step di Blasi constants were chosen as a lumped approximation for the overall reaction rate constant required for this nondimensional analysis.

$$Py_1 = \frac{k_{cond}}{k_{diBlasi}\rho_{part}C_p r^2} \quad (31)$$

A single-step pyrolysis reaction scheme is used here for simplicity rather than a multicomponent reaction scheme. The second pyrolysis number  $Py_2$ , eq 32, compares surface convective heat transfer with the effective reaction rate:

$$Py_2 = \frac{h_{conv}}{k_{diBlasi}\rho_{part}C_p r} \quad (32)$$

Six hypothetical cases representing a variety of pyrolysis regimes were explored to evaluate the impacts of anisotropic permeability, as shown in Table 2, by running two simulations: one with  $K_{rat} = 1$  and another with  $K_{rat} = 17,600$ , the measured value for pine as reported by Comstock.<sup>37</sup> Mettler et al.<sup>40</sup> expanded Pyle's and Zaror's work to a 2D pyrolysis regime

map that is useful here, as illustrated in Figure 6, for wood particles pyrolyzing at 500 °C. Case 1 is a small particle with high convective heat transfer coefficient ( $h$ ) in the isothermal reaction domain. Case 2 is a medium-sized particle with low  $h$  placing it in the convection-controlled regime. Cases 3 and 4 are small particles in the "noncontrolled" regime. Case 5 is a large particle with high  $h$  in the conduction-controlled regime, and Case 6 is small particle with high  $h$  that places it in the reaction-controlled regime. Under this framework, the oak particle lies in the "noncontrolled" regime, between convection and conduction control. Table 4 lists complete values and assigned regimes for each case.

Results shown in Figure 7 from the case studies (Table 4) expose the strongest influence of anisotropic permeability for the conduction-controlled parametrized model, wherein the 99% conversion time in the  $K_{rat} = 1$  case is more than five times that of  $K_{rat} = 17600$ ; the latter case is considered more physically relevant, as this permeability ratio has been measured experimentally for pine. Because internal conduction is the limiting heat transport mechanism for this large particle, convective flow of heat within the particle plays a larger role than for other cases. If just-reacted gases are advecting radially out of the biomass particle in the opposite direction as heat flux, this counteraction slows the rate of temperature rise driving the pyrolysis reactions. Cases 2–4, close to the convectively controlled regime, show minimal impact of specifying the permeability as isotropic vs anisotropic. Case 1 shows approximately 50% overestimate of conversion time for the isotropic case vs  $K_{rat} = 17600$ .

In order to further elucidate a regime map for conditions where accurate prediction of conversion time requires the inclusion of anisotropic convective transport properties, 79 cases were run with  $K_{rat}$  equal both to 1 and 17,600 for pine. Simulation parameters are shown in Table 3, while the heat transfer coefficient, particle radius, and density were modulated to span Biot and pyrolysis numbers from  $10 \times 10^{-2}$  to  $10 \times 10^2$ . Conversion times at 99% wood loss were interpolated into a color map shown in Figure 8.

From these results we can make the following general conclusions. (1) The influence of anisotropic permeability plays a notable role in conversion time when the Biot number is above 0.1 for all pyrolysis numbers, as well as when  $Py_2$  is less than 20. Here, using isotropic properties instead of anisotropic properties predicts more than 2 times the conversion time. (2) Pore structure most significantly impacts pyrolytic conversion time when the Biot number is above 1 and the  $Py_1$  number is below 1. Here, conversion time is overestimated by more than 8 times when isotropic properties are used. This effect is amplified as Bi increases and  $Py_1$  decreases together. These nondimensional numbers reflect the natural phenomenon that when internal heat conduction limits the overall rate of pyrolysis, off-gassing effectively lowers surface heat transfer rates by keeping the surface at the temperature that the gases escape. (3) This work affirms Di Blasi's insights that internal conduction dominates pyrolysis when the Biot number is high, and here is where pyrolysis models are sensitive to directional porosity.<sup>49</sup> However, the domain of significance is herein extended to where Biot number is greater than 0.1 and pyrolysis number is less than 20. No significant impact of pore structure was noticed when the Biot number is less than 0.1 or when the pyrolysis number is greater than 20 (Figure 8). Table 5 summarizes these results.

## 4. CONCLUSIONS

Historically, simplified biomass pyrolysis models ignore the mass source term of pyrolysis vapors being released inside the particle and advecting out of the biogenic and dynamic pore structure. While experimental results may often match the model well, this does not fully capture the nature of the concerted, coupled transport phenomena that occur during devolatilization. The present study provides some insights into nondimensional regimes where capturing the anisotropic pore structure is extremely important to ensure valid predictions, namely, the conduction-controlled regime and other regimes where it may be less important to capture this. These results can be used to simplify some modeling assumptions or even to revisit models that may have incorrectly acknowledged this effect. The authors recommend future investigations by the field to explore common but unique pore structures like biomass pellets, as well as to understand the dynamic evolution of pore structure and permeability during pyrolysis. The final pore structure of char may not have a major impact on devolatilization prediction accuracy, but when an oxidizer is present like in autothermal pyrolysis,<sup>6,52</sup> gasification, and combustion,<sup>29</sup> the char's porosity may strongly control particle oxidation. Kluska et al.<sup>53</sup> recently concluded that radial porosity is created during pyrolysis that allows gases to escape through the radius with particle experiments in the non-controlling regime. Further studies should also incorporate direct thermal measurements of biomass particles to evaluate the selection of internal thermal conductivity models. Ultimately, the anisotropic, feedstock-specific nature of permeability and heat transfer phenomena occurring during pyrolysis hold significant implications beyond the particle scale, influencing reactor design, unit throughput, and even capital intensity of the broader biorefinery. The conclusions reached in this study unravel yet more complexity behind these highly dynamic conversion strategies.

## AUTHOR INFORMATION

### Corresponding Author

**M. Brennan Pecha** – *Renewable Resources and Enabling Sciences Center, National Renewable Energy Laboratory, Golden, Colorado 80401, United States*; [orcid.org/0000-0002-0894-8504](https://orcid.org/0000-0002-0894-8504); Email: [brennan.pecha@nrel.gov](mailto:brennan.pecha@nrel.gov)

### Authors

**Nicholas E. Thornburg** – *Center for Integrated Mobility Sciences, National Renewable Energy Laboratory, Golden, Colorado 80401, United States*

**Chad A. Peterson** – *Department of Mechanical Engineering, Iowa State University, Ames, Iowa 50011, United States*

**Meagan F. Crowley** – *Renewable Resources and Enabling Sciences Center, National Renewable Energy Laboratory, Golden, Colorado 80401, United States*

**Xi Gao** – *National Energy Technology Laboratory, Morgantown, West Virginia 26507, United States; Leidos Research Support Team, Morgantown, West Virginia 26507, United States*

**Liqiang Lu** – *National Energy Technology Laboratory, Morgantown, West Virginia 26507, United States; Leidos Research Support Team, Morgantown, West Virginia 26507, United States*; [orcid.org/0000-0002-5101-1688](https://orcid.org/0000-0002-5101-1688)

**Gavin Wiggins** – *Oak Ridge National Laboratory, Oak Ridge, Tennessee 37830, United States*; [orcid.org/0000-0002-4737-6596](https://orcid.org/0000-0002-4737-6596)

**Robert C. Brown** – *Department of Mechanical Engineering, Iowa State University, Ames, Iowa 50011, United States; Bioeconomy Institute, Iowa State University, Ames, Iowa 50011, United States*; [orcid.org/0000-0003-0847-9557](https://orcid.org/0000-0003-0847-9557)

**Peter N. Ciesielski** – *Renewable Resources and Enabling Sciences Center, National Renewable Energy Laboratory, Golden, Colorado 80401, United States*; [orcid.org/0000-0003-3360-9210](https://orcid.org/0000-0003-3360-9210)

Complete contact information is available at: <https://pubs.acs.org/10.1021/acs.energyfuels.1c02679>

## Author Contributions

The manuscript was written through contributions of all authors. All authors have given approval to the final version of the manuscript.

## Notes

The authors declare no competing financial interest.

## ACKNOWLEDGMENTS

This work was authored in part by the National Renewable Energy Laboratory, operated by Alliance for Sustainable Energy, LLC, for the U.S. Department of Energy (DOE) under Contract No. DE-AC36-08GO28308. Funding is provided by U.S. Department of Energy Office of Energy Efficiency and Renewable Energy's Bioenergy Technologies Office. The views expressed in the article do not necessarily represent the views of the DOE or the U.S. Government. The U.S. Government retains and the publisher, by accepting the article for publication, acknowledges that the U.S. Government retains a nonexclusive, paid-up, irrevocable, worldwide license to publish or reproduce the published form of this work, or allow others to do so, for U.S. Government purposes. Special thanks to Jim Parks (ORNL) and Bill Rogers (NETL) for fruitful discussions and coordination regarding the background of this work. Special acknowledgement to P. Debiagi and T. Faravelli for help implementing the pyrolysis reaction scheme.

## ABBREVIATIONS

$\alpha$  = pyrolysis conversion from 0 to 1  
 Bi = Biot number  
 $C_j$  = concentration vapor species  $j$ , mol/m<sup>3</sup>  
 $C_i$  = concentration solid species  $i$ , mol/m<sup>3</sup>  
 $d$  = particle diameter, m  
 $D$  = gas diffusion tensor, m<sup>2</sup>/s  
 $c_{p,i/j}$  = heat capacity for each pseudospecies, J/mol K  
 $c_{p,solid/gas}$  = heat capacity of solid or gas, J/kg K  
 $\epsilon_g$  = particle porosity, i.e. void fraction  
 $h$  or  $htc$  = surface heat transfer coefficient, W/m<sup>2</sup> K  
 $K$  = intraparticle permeability tensor, m<sup>2</sup>  
 $K_{ax}$  = axial permeability along the pores, m<sup>2</sup>  
 $K_{rad}$  = radial permeability across the pores, m<sup>2</sup>  
 $K_{rat} = K_{axial}/K_{rad}$   
 $k_{eff}$  = effective thermal conductivity tensor for the particle, W/m K  
 $L$  = cylindrical particle length, m  
 $M_w$  = molecular weight, kg/m<sup>3</sup>  
 $Py_1$  = pyrolysis number 1  
 $Py_2$  = pyrolysis number 2  
 $p$  = pressure, pa  
 $Q$  = heat source term  
 $Q_m$  = mass source term  
 $r$  = cylindrical particle radius, m

$R_j$  = reaction rate for species  $j$   
 $\rho_g$  = fluid density, kg/m<sup>3</sup>  
 $\rho_s$  = solids density, kg/m<sup>3</sup>  
 $\rho_{s,0}$  = initial solids density, kg/m<sup>3</sup>  
 $t$  = time, s  
 $T$  = temperature, K  
 $T_{inf}$  = free stream gas temperature, K  
 $u$  = gas velocity vector, m/s

## REFERENCES

- (1) Griffin, M. B.; Iisa, K.; Wang, H.; Dutta, A.; Orton, K. A.; French, R. J.; Santosa, D. M.; Wilson, N.; Christensen, E.; Nash, C.; Van Allsburg, K. M.; Baddour, F. G.; Ruddy, D. A.; Tan, E. C. D.; Cai, H.; Mukarakate, C.; Schaidle, J. A. Driving towards cost-competitive biofuels through catalytic fast pyrolysis by rethinking catalyst selection and reactor configuration. *Energy Environ. Sci.* **2018**, *11* (10), 2904–2918.
- (2) Eschenbacher, A.; Saraeian, A.; Shanks, B. H.; Jensen, P. A.; Li, C.; Duus, J. Ø.; Hansen, A. B.; Mentzel, U. V.; Henriksen, U. B.; Ahrenfeldt, J.; Jensen, A. D. Enhancing bio-oil quality and energy recovery by atmospheric hydrodeoxygenation of wheat straw pyrolysis vapors using Pt and Mo-based catalysts. *Sustainable Energy & Fuels* **2020**, *4* (4), 1991–2008.
- (3) Wang, H.; Lee, S.-J.; Olarte, M. V.; Zacher, A. H. Bio-oil Stabilization by Hydrogenation over Reduced Metal Catalysts at Low Temperatures. *ACS Sustainable Chem. Eng.* **2016**, *4* (10), 5533–5545.
- (4) Debiagi, P. E. A.; Pecchi, C.; Gentile, G.; Frassoldati, A.; Cuoci, A.; Faravelli, T.; Ranzi, E. Extractives Extend the Applicability of Multistep Kinetic Scheme of Biomass Pyrolysis. *Energy Fuels* **2015**, *29* (10), 6544–6555.
- (5) Santamaria, L.; Beirou, M.; Mangold, F.; Lopez, G.; Olazar, M.; Schmid, M.; Li, Z.; Scheffknecht, G. Influence of temperature on products from fluidized bed pyrolysis of wood and solid recovered fuel. *Fuel* **2021**, *283*, 118922.
- (6) Polin, J. P.; Peterson, C. A.; Whitmer, L. E.; Smith, R. G.; Brown, R. C. Process intensification of biomass fast pyrolysis through autothermal operation of a fluidized bed reactor. *Appl. Energy* **2019**, *249*, 276–285.
- (7) Zhou, S.; Garcia-Perez, M.; Pecha, B.; McDonald, A. G.; Westerhof, R. J. M. Effect of particle size on the composition of lignin derived oligomers obtained by fast pyrolysis of beech wood. *Fuel* **2014**, *125*, 15–19.
- (8) Shen, J.; Wang, X.-S.; Garcia-Perez, M.; Mourant, D.; Rhodes, M. J.; Li, C.-Z. Effects of particle size on the fast pyrolysis of oil mallee woody biomass. *Fuel* **2009**, *88* (10), 1810–1817.
- (9) Kersten, S. R. A.; Wang, X.; Prins, W.; van Swaaij, W. P. M. Biomass Pyrolysis in a Fluidized Bed Reactor. Part 1: Literature Review and Model Simulations. *Ind. Eng. Chem. Res.* **2005**, *44* (23), 8773–8785.
- (10) Lu, L.; Gao, X.; Shahnam, M.; Rogers, W. A. Bridging particle and reactor scales in the simulation of biomass fast pyrolysis by coupling particle resolved simulation and coarse grained CFD-DEM. *Chem. Eng. Sci.* **2020**, *216*, 115471.
- (11) Pecha, M. B.; Arbelaez, J. I. M.; Garcia-Perez, M.; Chejne, F.; Ciesielski, P. N. Progress in understanding the four dominant intraparticle phenomena of lignocellulose pyrolysis: chemical reactions, heat transfer, mass transfer, and phase change. *Green Chem.* **2019**, *21* (11), 2868–2898.
- (12) Mettler, M. S.; Mushrif, S. H.; Paulsen, A. D.; Javadekar, A. D.; Vlachos, D. G.; Dauenhauer, P. J. Revealing pyrolysis chemistry for biofuels production: Conversion of cellulose to furans and small oxygenates. *Energy Environ. Sci.* **2012**, *5* (1), 5414–5424.
- (13) Van de Velden, M.; Baeyens, J.; Brems, A.; Janssens, B.; Dewil, R. Fundamentals, kinetics and endothermicity of the biomass pyrolysis reaction. *Renewable Energy* **2010**, *35* (1), 232–242.
- (14) Antal, M. J.; Varhegyi, G.; Jakab, E. Cellulose pyrolysis kinetics: Revisited. *Ind. Eng. Chem. Res.* **1998**, *37* (4), 1267–1275.
- (15) Iisa, K.; French, R. J.; Orton, K. A.; Dutta, A.; Schaidle, J. A. Production of low-oxygen bio-oil via ex situ catalytic fast pyrolysis and hydrotreating. *Fuel* **2017**, *207*, 413–422.
- (16) Anex, R. P.; Aden, A.; Kazi, F. K.; Fortman, J.; Swanson, R. M.; Wright, M. M.; Satrio, J. A.; Brown, R. C.; Daugaard, D. E.; Platon, A.; Kothandaraman, G.; Hsu, D. D.; Dutta, A. Techno-economic comparison of biomass-to-transportation fuels via pyrolysis, gasification, and biochemical pathways. *Fuel* **2010**, *89*, S29–S35.
- (17) Di Blasi, C.; Branca, C.; Lombardi, V.; Ciappa, P.; Di Giacomo, C. Effects of Particle Size and Density on the Packed-Bed Pyrolysis of Wood. *Energy Fuels* **2013**, *27* (11), 6781–6791.
- (18) Ciesielski, P. N.; Pecha, M. B.; Lattanzi, A. M.; Bharadwaj, V. S.; Crowley, M. F.; Bu, L.; Vermaas, J. V.; Steirer, K. X.; Crowley, M. F. Advances in Multiscale Modeling of Lignocellulosic Biomass. *ACS Sustainable Chem. Eng.* **2020**, *8* (9), 3512–3531.
- (19) Xiong, Q.; Xu, F.; Pan, Y.; Yang, Y.; Gao, Z.; Shu, S.; Hong, K.; Bertrand, F.; Chaouki, J. Major trends and roadblocks in CFD-aided process intensification of biomass pyrolysis. *Chem. Eng. Process.* **2018**, *127*, 206–212.
- (20) Ciesielski, P. N.; Pecha, M. B.; Bharadwaj, V. S.; Mukarakate, C.; Leong, G. J.; Kappes, B.; Crowley, M. F.; Kim, S.; Foust, T. D.; Nimlos, M. R. Advancing catalytic fast pyrolysis through integrated multiscale modeling and experimentation: Challenges, progress, and perspectives. *Wiley Interdiscip. Rev.: Energy Environ.* **2018**, *7* (4), No. e297.
- (21) Pyle, D. L.; Zaror, C. A. Heat transfer and kinetics in the low temperature pyrolysis of solids. *Chem. Eng. Sci.* **1984**, *39* (1), 147–158.
- (22) Di Blasi, C. Heat transfer mechanisms and multi-step kinetics in the ablative pyrolysis of cellulose. *Chem. Eng. Sci.* **1996**, *51*, 2211–2220.
- (23) Di Blasi, C. Modeling Chemical and Physical Processes of Wood and Biomass Pyrolysis. *Prog. Energy Combust. Sci.* **2008**, *34* (1), 47–90.
- (24) Di Blasi, C. Modeling Intra- and Extra-Particle Processes of Wood Fast Pyrolysis. *AIChE J.* **2002**, *48* (10), 2386–2397.
- (25) Debiagi, P.; Gentile, G.; Cuoci, A.; Frassoldati, A.; Ranzi, E.; Faravelli, T. A predictive model of biochar formation and characterization. *J. Anal. Appl. Pyrolysis* **2018**, *134*, 326–335.
- (26) Gentile, G.; Debiagi, P. E. A.; Cuoci, A.; Frassoldati, A.; Ranzi, E.; Faravelli, T. A computational framework for the pyrolysis of anisotropic biomass particles. *Chem. Eng. J.* **2017**, *321*, 458–473.
- (27) Ranzi, E.; Cuoci, A.; Faravelli, T.; Frassoldati, A.; Migliavacca, G.; Pierucci, S.; Sommariva, S. Chemical Kinetics of Biomass Pyrolysis. *Energy Fuels* **2008**, *22* (6), 4292–4300.
- (28) Anca-Couce, A.; Sommersacher, P.; Scharler, R. Online experiments and modelling with a detailed reaction scheme of single particle biomass pyrolysis. *J. Anal. Appl. Pyrolysis* **2017**, *127*, 411–425.
- (29) Anca-Couce, A.; Caposciutti, G.; Gruber, T.; Kelz, J.; Bauer, T.; Hochenaue, C.; Scharler, R. Single large wood log conversion in a stove: Experiments and modelling. *Renewable Energy* **2019**, *143*, 890–897.
- (30) Anca-Couce, A.; Zobel, N. Numerical analysis of a biomass pyrolysis particle model: Solution method optimized for the coupling to reactor models. *Fuel* **2012**, *97*, 80–88.
- (31) Pecha, M. B.; Ramirez, E.; Wiggins, G. M.; Carpenter, D.; Kappes, B.; Daw, S.; Ciesielski, P. N. Integrated Particle- and Reactor-Scale Simulation of Pine Pyrolysis in a Fluidized Bed. *Energy Fuels* **2018**, *32* (10), 10683–10694.
- (32) Ciesielski, P. N.; Wiggins, G. M.; Jakes, J. E.; Daw, C. S. Simulating Biomass Fast Pyrolysis at the Single Particle Scale. In *Fast Pyrolysis of Biomass: Advances in Science and Technology*; Royal Society of Chemistry, 2017; pp 231–253.
- (33) Ciesielski, P. N.; Crowley, M.; Nimlos, M.; Sanders, A.; Wiggins, G.; Robichaud, D.; Donohoe, B.; Foust, T. Biomass Particle Models with Realistic Morphology and Resolved Microstructure for Simulations of Intraparticle Transport Phenomena. *Energy Fuels* **2015**, *29* (1), 242–254.

- (34) Vay, O.; De Borst, K.; Hansmann, C.; Teischinger, A.; Müller, U. Thermal conductivity of wood at angles to the principal anatomical directions. *Wood Sci. Technol.* **2015**, *49* (3), 577–589.
- (35) Hankalin, V.; Ahonen, T.; Raiko, R. On thermal properties of a pyrolysing wood particle. In *Finnish-Swedish Flame Days*, 2009.
- (36) Di Blasi, C. Influences of physical properties on biomass devolatilization characteristics. *Fuel* **1997**, *76* (10), 957–964.
- (37) Comstock, G. L. Directional permeability of softwoods. *Wood Fiber Sci.* **1970**, *1* (4), 283–289.
- (38) Di Blasi, C. Physico-chemical processes occurring inside a degrading two-dimensional anisotropic porous medium. *Int. J. Heat Mass Transfer* **1998**, *41* (24), 4139–4150.
- (39) Paulsen, A. D.; Mettler, M. S.; Dauenhauer, P. J. The Role of Sample Dimension and Temperature in Cellulose Pyrolysis. *Energy Fuels* **2013**, *27* (4), 2126–2134.
- (40) Mettler, M. S.; Vlachos, D. G.; Dauenhauer, P. J. Top Ten Fundamental Challenges of Biomass Pyrolysis for Biofuels. *Energy Environ. Sci.* **2012**, *5* (7), 7797–7809.
- (41) Wiggins, G. M.; Ciesielski, P. N.; Daw, C. S. Low-Order Modeling of Internal Heat Transfer in Biomass Particle Pyrolysis. *Energy Fuels* **2016**, *30* (6), 4960–4969.
- (42) Tavassoli, H.; Peters, E. A. J. F.; Kuipers, J. A. M. Direct numerical simulation of fluid–particle heat transfer in fixed random arrays of non-spherical particles. *Chem. Eng. Sci.* **2015**, *129*, 42–48.
- (43) Pecha, M. B.; Garcia-Perez, M.; Foust, T. D.; Ciesielski, P. N. Estimation of Heat Transfer Coefficients for Biomass Particles by Direct Numerical Simulation Using Microstructured Particle Models in the Laminar Regime. *ACS Sustainable Chem. Eng.* **2017**, *5* (1), 1046–1053.
- (44) Coker, A. K. *Ludwig's Applied Process Design for Chemical and Petrochemical Plants*; Gulf Professional Publishing, 2014.
- (45) Bellais, M. *Modelling of the Pyrolysis of Large Wood Particles*. Dissertation, KTH: Stockholm, 2007.
- (46) Weatherwax, R.; Tarkow, H. Density of wood substance. Importance of penetration and adsorption compression of the displacement fluid. *For. Prod. J.* **1968**, *18* (7), 44–46.
- (47) Hunt, J. F.; Gu, H.; Lebow, P. K. Theoretical thermal conductivity equation for uniform density wood cells. *Wood Fiber Sci.* **2008**, *40* (2), 167–180.
- (48) Lindstrom, J. K.; Proano-Aviles, J.; Johnston, P. A.; Peterson, C. A.; Stansell, J. S.; Brown, R. C. Competing reactions limit levoglucosan yield during fast pyrolysis of cellulose. *Green Chem.* **2019**, *21* (1), 178–186.
- (49) Di Blasi, C. Physico-chemical processes occurring inside a degrading two-dimensional anisotropic porous medium. *Int. J. Heat Mass Transfer* **1998**, *41* (24), 4139–4150.
- (50) Wardach-Swięcicka, I.; Kardaś, D. Modelling thermal behaviour of a single solid particle pyrolysing in a hot gas flow. *Energy* **2021**, *221*, 119802.
- (51) Di Blasi, C.; Branca, C. Kinetics of primary product formation from wood pyrolysis. *Ind. Eng. Chem. Res.* **2001**, *40* (23), 5547–5556.
- (52) Brown, R. C. Process Intensification through Directly Coupled Autothermal Operation of Chemical Reactors. *Joule* **2020**, *4* (11), 2268–2289.
- (53) Kluska, J.; Ronewicz, K.; Kardaś, D. Thermal characteristics of single wood particle pyrolysis using particle image velocimetry. *Int. J. Therm. Sci.* **2019**, *135*, 276–284.